Fabric-based modeling of thermo-mechanical damage and healing around salt caverns

C. Zhu & C. Arson
Geosystems group, School of Civil and Environmental Engineering,
Georgia Institute of Technology, Atlanta, Georgia, USA.

ABSTRACT: Geotechnical reservoirs and repositories in salt such as nuclear waste disposals, geothermal systems, and compressed air energy storage (CAES) are usually subject to complex thermo-mechanical conditions, leading to crack initiation, propagation, and rebonding. This work aims to model thermo-mechanical damage and healing around salt caverns, by enriching the framework of continuum damage mechanics with fabric descriptors. In order to infer the form of fabric tensors from microstructure observations, we carry out creep tests on granular salt under constant stress and humidity conditions. We simulate a stress path typical of CAES conditions at the material element level. The model presented in this paper is expected to improve the fundamental understanding of damage and healing in rocks at both macroscopic and microscopic levels, and the long-term evaluation of geological storage facilities.

1 INTRODUCTION

Damage initiation and evolution are critical issues for the design and long-term assessment of nuclear waste disposals and compressed air energy storage (CAES) facilities, which usually undergo high stress and temperature gradients. Salt rock is an attractive host rock for geological storage.

Most damage and healing models proposed in rock thermo-mechanics are based on the concept of dilatancy boundary (Hou 2003). Anisotropic healing models based on Continuum Damage Mechanics (CDM) usually resort to the concept of "net damage", which allows modeling stiffness degradation (damage) and recovery (healing). These theoretical frameworks are purely hypothetical and do not allow the prediction of all coupled processes that occur in actual rock materials. Rock damage models distinguishing closure and rebonding conveniently model all dissipation processes with rate-dependent evolution laws, which avoids enforcing the positivity of the dissipation potential. Unfortunately, such models do not properly represent the brittle behavior resulting from rate-independent crack opening and closure: Healing is actually considered as a particular form of crack closure (detected by an increase of wave velocity) rather than crack rebonding.

This study aims to enrich a continuum thermo-mechanical framework of anisotropic damage mechanics fabric descriptors, in order to link macroscopic deformation and stiffness degradation to rock microstructure evolution, and to distinguish unilateral effects (due to crack closure) from mechanical recovery (due to crack rebonding). Two types of self-healing systems have been recognized so far, including a coupled system triggered by damage mechanics, and a de-coupled system relying upon external triggering. The model proposed in this study belongs to the category of de-coupled passive system, analogous to the close-then-heal scheme (Li & Uppu 2010). Healing is attributed to intra-granular Diffusive Mass Transfer (DMT). We reckon that this assumption ignores healing anisotropy due to grain-boundary diffusion and recrystallization: These two phenomena will be accounted for in a future model that will couple thermo-mechanical damage and healing to solid-fluid chemical interactions (between salt crystals and saturating brine).

Section 2 explains how we chose fabric descriptors, based on an image analysis of granular salt subject to creep tests. Section 3 presents the multi-scale theoretical model of damage and healing, coupling crack opening, closure, and healing. Section 4 summarizes the results of simulations performed at the material element level, in typical CAES conditions.

2 MICROSTRUCTURE CHARACTERIZATION

Table salt has the same crystallographic structure and halite content as salt rock. In this study, we conducted microscopic observations in table salt during creep tests, in order to characterize microstructure changes with ad hoc mathematical descriptors. In the experiment, salt grains were confined in tubes with both ends fixed by nails (Fig. 1). The tubes were placed in a humidity-controlled chamber. Constant humidity was ensured by adding saturated salt water to the bottom of the chamber, as explained in (Wexler & Hasegawa 1954). Three constant compressive loads were applied by controlling the elongation of springs of the same rigidity. During the creep tests, we noted that the deformed spring length was almost unchanged, which allowed us to assume that the axial stress imposed at the boundary was constant.

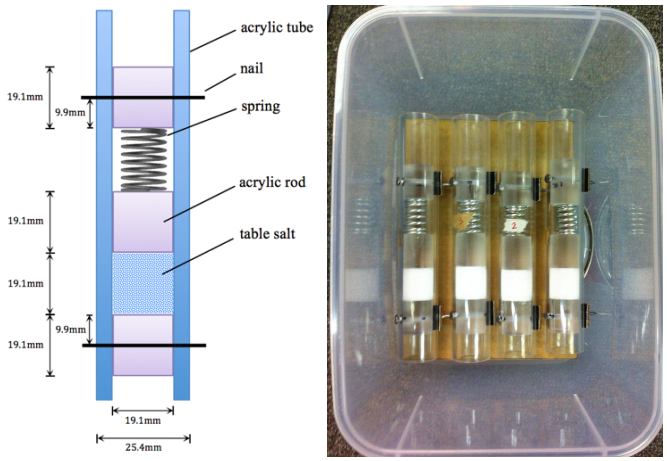

Figure 1. Experimental set up for the creep test performed on table salt.

We recorded microscopic images of salt at regular time intervals (Fig. 2a). The *ImageJ* application developed by Abramoff et al. (2004) was used to process the microscopic images, following the steps shown in Figure 2 Enhancing the contrast and removing the background provided a preliminary binary image (Fig. 2b). However, transparent salt particles reflect light at their planar surfaces and transmit light through their bulks, which impaired the image quality during the stereoscopic observations. Removing outliers and filtering procedure helped improving the quality of images. In Figure 2c, the black regions indicate the presence of void space between salt grains. Then we plotted the probability density functions of several geometric descriptors such as void area, axis lengths of various shapes fitting in the voids, and branch lengths (Fig. 2d).

Through testing of several shapes, fitting ellipses presented the best match with void contours. Statistical results indicated that the probability density function of ellipses' area (void area) follows a power law (Fig. 3a) as

$$p_A(A_v) = a \cdot A_v^t. \quad (1)$$

For high values of void area (A_v), the power law did not fit the experimental data as well as for small values of void area. Since the probability density function is in a log scale, this error was however considered acceptable. After fitting the plot of the probability density function to the microscopic data, we obtained: $a = 5\times10^{-5}$ and $t = -1.2$.

The projections of ellipses' semi-axes in the three principal directions of space (defined as crack lengths) were found to obey a lognormal distribution (Fig. 3b) as

$$p_i(R_i) = \frac{1}{\sqrt{2\pi}R_i s_i} e^{-\frac{(lnR_i - m_i)^2}{2s_i^2}}, \quad (2)$$

in which s_i is the standard deviation and m_i is the mean value. Note that the spikes in Figure 3b are attributed to an insufficient quality of the binary image – image analysis improvements are on-going.

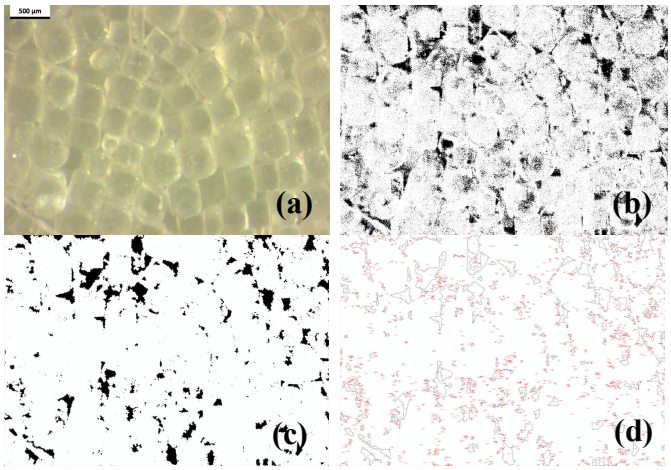

Figure 2. Image processing: (a) stereo-microscopic image; (b) binary image; (c) void distribution after the filter process; (d) void contours.

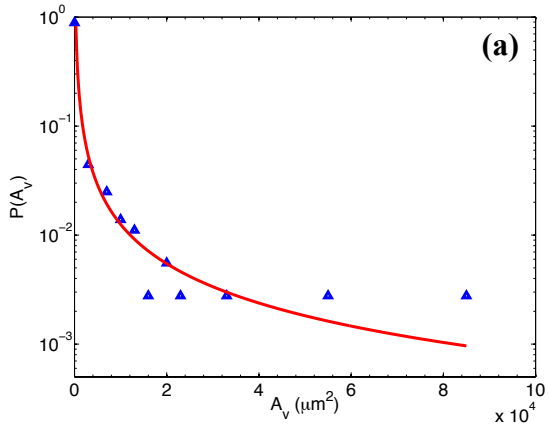

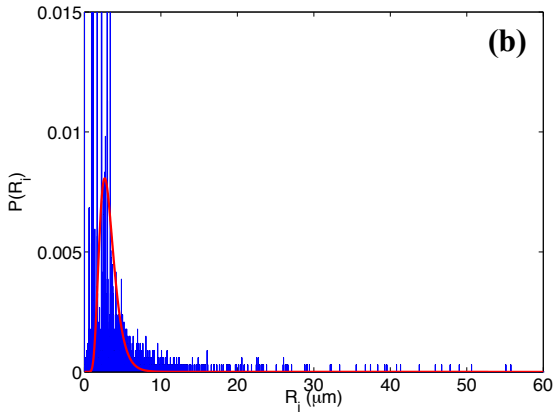

Figure 3. Probability density functions: (a) void area distribution; (b) crack length distribution.

Long-term qualitative microscopic observation substantiates that salt grains tend to rearrange to ordered packing and rebond at their boundaries (Fig. 4).

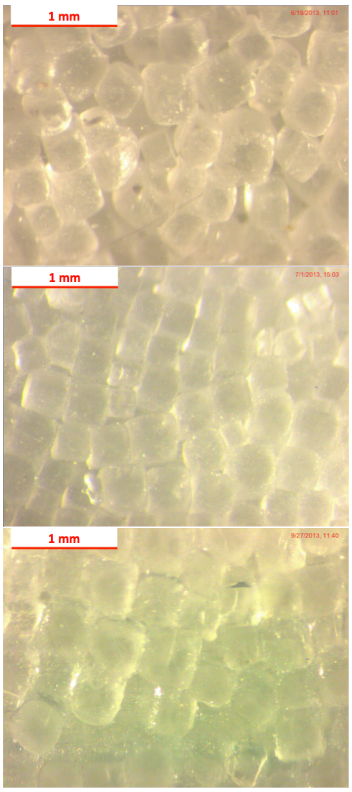

Figure 4. Fabric change in salt grains under stereo-microscopic observation (after 18, 31, and 120 days, respectively).

3 THEORETICAL FRAMEWORK

3.1 *Continuum Damage Model*

The proposed damage and healing model couples microscopic and macroscopic thermo-mechanical evolution laws, in order to capture the influence of microscopic debonding, opening, closure and rebonding on deformation and stiffness. We use the CDM framework developed previously by Zhu & Arson (2014a) as a basis to model rock damaged macroscopic behavior (Table 1).

We decompose the total deformation into three components, as shown in the typical loading-unloading stress-strain plot (Fig. 5). $\boldsymbol{\varepsilon^{el}}$ is the purely elastic deformation - recoverable upon unloading. $\boldsymbol{\varepsilon^{d}}$ is the damage deformation, which has two components: $\boldsymbol{\varepsilon^{ed}}$ is the damage-induced elastic deformation (induced by the degradation of stiffness); $\boldsymbol{\varepsilon^{id}}$ is the irreversible deformation due to residual crack openings. The summation of $\boldsymbol{\varepsilon^{el}}$ and $\boldsymbol{\varepsilon^{ed}}$ gives the total elastic deformation $\boldsymbol{\varepsilon^{E}}$. The additional compression stress required to compensate $\boldsymbol{\varepsilon^{id}}$ is known as the residual stress:

$$\boldsymbol{\sigma_R} = -\boldsymbol{D}(\boldsymbol{\Omega}) : \boldsymbol{\varepsilon^{id}}, \tag{3}$$

in which $\boldsymbol{D}$ is the stiffness tensor, $\boldsymbol{D_0}$ is the reference stiffness in the undamaged state, and $\boldsymbol{\Omega}$ is the damage variable.

The free energy of the solid skeleton consists of the purely thermo-elastic deformation energy (ψ_s^{ET}) and the potential energy of crack faces ($\psi_s^{\Omega T}$).

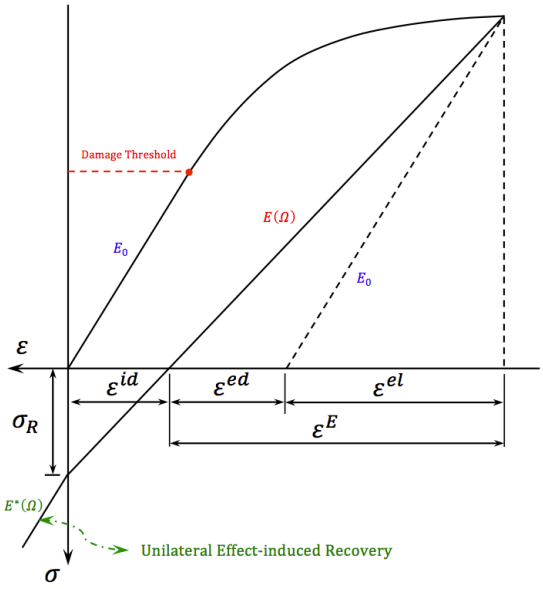

Figure 5. Decomposition of deformation with soil mechanics sign convention (compression counted positive).

Thermodynamic conjugation relationships yield the stress and the damage driving force (Collins & Houlsby 1997). A dimensional analysis shows that the quadratic term in temperature $\frac{\tau^2}{2\tau_0}\frac{\partial C(\boldsymbol{\Omega})}{\partial \boldsymbol{\Omega}}$ is negligible. For simplicity, the damage criterion is independent of temperature variation. The active damage driving force ($\boldsymbol{Y_d}$) is further simplified as a function of total strain only.

The damage criterion is expressed in the form of a norm minus the damage threshold (Table 1), which accounts for hardening: The release of energy needed to propagate damage increases as damage accumulates, and decreases as temperate increases.

Following a classical CDM assumption (Dragon et al. 2000), we assume the damage flow rule to be associative, i.e., f_d is used as the damage potential:

$$d\boldsymbol{\Omega} = d\lambda_d \frac{\partial f_d(\boldsymbol{Y_d},\boldsymbol{\Omega})}{\partial \boldsymbol{Y_d}} = \frac{[\frac{\boldsymbol{Y_d}}{\sqrt{2\boldsymbol{Y_d}:\boldsymbol{Y_d}}}]:d\boldsymbol{Y_d}}{(C_1\boldsymbol{\delta}):[\frac{\boldsymbol{Y_d}}{\sqrt{2\boldsymbol{Y_d}:\boldsymbol{Y_d}}}]} : [\frac{\boldsymbol{Y_d}}{\sqrt{2\boldsymbol{Y_d}:\boldsymbol{Y_d}}}]. \quad (4)$$

Cracks are considered as closed when their faces are in contact but not bonded. We adopt the concept of unilateral effect in order to account for the recovery of material compressive strength due to closure of tensile cracks. Following Chaboche's (1992) approach, stiffness depends on a Heaviside function to distinguish the behaviors in tension and compression. Crack closure increases the number of intergranular contacts in the Representative Element Volume (REV), which increases stiffness ($\boldsymbol{D}^*(\boldsymbol{\Omega})$) as well as heat capacity ($C^*(\boldsymbol{\Omega})$) (Table 1).

3.2 *Diffusive Mass Transfer-induced Healing*

We considered damage as a rate-independent dissipation variable. The consistency equation imposes that damage cannot decrease. To represent the difference between damage and healing, we introduced a mixed damage variable $\boldsymbol{A}$ (Table 1). So the expressions of the recovered stiffness and heat capacity depend on $\boldsymbol{A}$ instead of $\boldsymbol{\Omega}$. Healing does not occur upon bare crack closure: DMT is the main driving factor for crack rebonding at elevated temperature (Senseny et al. 1992, Fam et al. 1998). An energy input is required to trigger the migration of ions within the lattice. Healing is therefore a dissipative process, independent from damage (Arson et al. 2012). Cracks heal when surface tension decreases, crack contact areas increase, and electronic forces attract different ionic species at the crack faces (Fuenkajorn & Phueakphum 2011, Houben et al. 2013). Because of the uniform distribution of grain orientations, we assumed that the intra-granular diffusion as an isotropic phenomenon, which allows defining the healing tensor as a scalar: $\boldsymbol{H} = h\boldsymbol{\delta}$.

The migration of sodium ions from salt grain bulk to grain boundaries is governed by a diffusion equation. Accordingly, we assumed that the intensity of

Table 1. Outline of thermo-mechanical damage and healing model

Postulates	
Free Energy for Crack Opening (Ψ_S)	$\psi_s = \psi_s^{ET} + \psi_s^{\Omega T} = \left[\frac{1}{2}\boldsymbol{\varepsilon^{el}}:\boldsymbol{D_0}:\boldsymbol{\varepsilon^{el}} - \frac{C_0\tau^2}{2\tau_0} - \tau\boldsymbol{K_0}:\boldsymbol{\varepsilon^{el}}\right] + [\frac{1}{2}\boldsymbol{\varepsilon^d}:\boldsymbol{D}(\boldsymbol{\Omega}):\boldsymbol{\varepsilon^d} - \frac{C(\boldsymbol{\Omega})\tau^2}{2\tau_0} - \tau\boldsymbol{K}(\boldsymbol{\Omega}):\boldsymbol{\varepsilon^d}]$ $\frac{1}{2}\boldsymbol{\varepsilon^d}:\boldsymbol{D}(\boldsymbol{\Omega}):\boldsymbol{\varepsilon^d} = \frac{1}{2}\lambda\left(tr\boldsymbol{\varepsilon^d}\right)^2 + \mu tr\left(\boldsymbol{\varepsilon^d}\cdot\boldsymbol{\varepsilon^d}\right) + \alpha tr\boldsymbol{\varepsilon^d} tr\left(\boldsymbol{\varepsilon^d}\cdot\boldsymbol{\Omega}\right) + 2\beta tr(\boldsymbol{\varepsilon^d}\cdot\boldsymbol{\varepsilon^d}\cdot\boldsymbol{\Omega})$
Free Energy for Crack Closure (Ψ_S)	$\psi_s = \left[\frac{1}{2}\boldsymbol{\varepsilon^{el}}:\boldsymbol{D_0}:\boldsymbol{\varepsilon^{el}} - \frac{C_0\tau^2}{2\tau_0} - \tau\boldsymbol{K_0}:\boldsymbol{\varepsilon^{el}}\right] + [\frac{1}{2}\boldsymbol{\varepsilon^d}:\boldsymbol{D^*}(\boldsymbol{\Omega}):\boldsymbol{\varepsilon^d} - \frac{C^*(\boldsymbol{\Omega})\tau^2}{2\tau_0} - \tau\boldsymbol{K^*}(\boldsymbol{\Omega}):\boldsymbol{\varepsilon^d}]$ $\boldsymbol{D^*}(\boldsymbol{\Omega}) = \boldsymbol{D}(\boldsymbol{\Omega}) + \eta\sum_{i=1}^{3} H\left(-tr(\boldsymbol{P}_i:\boldsymbol{\varepsilon})\right)\boldsymbol{P}_i:\left(\boldsymbol{D_0} - \boldsymbol{D}(\boldsymbol{\Omega})\right):\boldsymbol{P}_i,\ 0<\eta\le 1$ $\boldsymbol{K^*}(\boldsymbol{\Omega}) = \boldsymbol{K}(\boldsymbol{\Omega}) + \eta\sum_{i=1}^{3} H\left(-tr(\boldsymbol{P}_i:\boldsymbol{\varepsilon})\right)\boldsymbol{P}_i:\left(\boldsymbol{K_0} - \boldsymbol{K}(\boldsymbol{\Omega})\right):\boldsymbol{P}_i,\ 0<\eta\le 1$ $C^*(\boldsymbol{\Omega}) = C(\boldsymbol{\Omega}) + \eta\sum_{i=1}^{3} H\left(-tr(\boldsymbol{P}_i:\boldsymbol{\varepsilon})\right)\boldsymbol{P}_i:\left[\left(C_0 - C(\boldsymbol{\Omega})\right)\boldsymbol{\delta}\otimes\boldsymbol{\delta}\right]:\boldsymbol{P}_i,\ 0<\eta\le 1$
Free Energy for Crack Rebonding (Ψ_S)	Replace $\boldsymbol{\Omega}$ by $\boldsymbol{A}$ in the free energy for crack closure $\boldsymbol{A} = \boldsymbol{\Omega} - \boldsymbol{\delta}h$
Damage Criterion (f_d)	$f_d(\boldsymbol{Y_d},\boldsymbol{\Omega}) = \sqrt{\frac{1}{2}\boldsymbol{Y_d}:\boldsymbol{Y_d}} - [a_0 + a_1\mathrm{tr}(\boldsymbol{\Omega})]$
Strain Decomposition	$\boldsymbol{\varepsilon} = \boldsymbol{\varepsilon^E} + \boldsymbol{\varepsilon^{id}} = \boldsymbol{\varepsilon^{el}} + \boldsymbol{\varepsilon^d} = \boldsymbol{\varepsilon^{el}} + \boldsymbol{\varepsilon^{ed}} + \boldsymbol{\varepsilon^{id}}$
Diffusion Equation	$\bar{u}(t) = < u(x,t) > = \frac{1}{l}\int_0^l u(x,t)dx = \frac{8U_0}{\pi l}\sum_{i=1,3,5,\dots}^{\infty}\frac{e^{-\lambda_n^2 D_c t}}{n\lambda_n}$ $D_c = D_{c0}e^{-\frac{Q}{RT}}$, $h(t) = 1 - \bar{u}(t)$
Conjugation relationships	
Stress ($\boldsymbol{\sigma}$)	$\boldsymbol{\sigma} = \frac{\partial\psi_S}{\partial\boldsymbol{\varepsilon^{el}}} = \boldsymbol{D_0}:\boldsymbol{\varepsilon^{el}} - \tau\boldsymbol{K_0}$
Damage Driving Force ($\boldsymbol{Y_d}$)	$\boldsymbol{Y} = -\frac{\partial\psi_S}{\partial\boldsymbol{\Omega}} = -\left[\boldsymbol{D}(\boldsymbol{\Omega}):\boldsymbol{\varepsilon^d}\right]:\frac{\partial\boldsymbol{\varepsilon^d}}{\partial\boldsymbol{\Omega}} - \frac{1}{2}\boldsymbol{\varepsilon^d}:\frac{\partial\boldsymbol{D}(\boldsymbol{\Omega})}{\partial\boldsymbol{\Omega}}:\boldsymbol{\varepsilon^d} + \frac{\tau^2}{2\tau_0}\frac{\partial C(\boldsymbol{\Omega})}{\partial\boldsymbol{\Omega}} + \tau\boldsymbol{K}(\boldsymbol{\Omega}):\frac{\partial\boldsymbol{\varepsilon^d}}{\partial\boldsymbol{\Omega}} + \tau\frac{\partial\boldsymbol{K}(\boldsymbol{\Omega})}{\partial\boldsymbol{\Omega}}:\boldsymbol{\varepsilon^d}$ $\boldsymbol{Y_d} = -(\alpha+2\beta)\boldsymbol{\varepsilon}\cdot\boldsymbol{\varepsilon}$

α,β	mechanical damage parameters	a_0	initial damage threshold
λ,μ	Lamé coefficients	a_1	damage hardening parameter
τ_0	initial temperature	g	toughness parameter
$\boldsymbol{D}$	damaged stiffness tensor	k	bulk modulus
α_T	thermal expansion coefficient	$\boldsymbol{K}$	$k\alpha_T$ "diagonal tensor"
$\boldsymbol{D}^*$	effective stiffness tensor after "partial recovery"	C	damaged heat capacity
$\boldsymbol{K}^*$	effective diagonal tensor after "partial recovery"	A	TM damage parameter
C^*	effective heat capacity after "partial recovery"	η	degree of maximum stiffness recovery
$\boldsymbol{P_i}$	4th order project tensor for the projection in crack planes normal to direction i	$\boldsymbol{\delta}$	second order identity tensor

net damage, defined as $u = U_0 - h$, satisfies the following diffusion equation:

$$\frac{\partial u}{\partial t} = D_c \nabla^2 u, \quad (5)$$

in which D_c is the diffusion coefficient and U_0 is the intensity of damage in the REV before healing occurs:

$$U_0 = tr(\Omega)_{t=0}, \quad (6)$$

The maximum diffusion distance is half of the edge length of a grain. Crack healing is complete when an ion reaches a crack face and electronic forces bonds this ion to the lattice of the opposite crack face. At the boundaries, the net damage is zero. The initial conditions for healing in the REV are

$$h(x, t = 0) = 0, \quad u(x, t = 0) = U_0. \quad (7)$$

Therefore, the solution of Equation 5 is

$$u(x,t) = \frac{4U_0}{\pi} \sum_{i=1,3,5,\dots}^{\infty} \frac{e^{-\lambda_n^2 D_c t} \sin(\lambda_n x)}{n}, \quad (8)$$

in which $\lambda_n = \frac{n\pi}{l}$.

range: 573K ~ 973K), a linear relation can be established between the diffusion coefficient and temperature, as

$$D_c = -\frac{1.67\times10^{-12}}{T} + 2.99\times10^{-15}, \quad (9)$$

in which T is expressed in Kelvin and D_c is in m^2/s.

3.3 *Upscaling Method*

We considered granular salt creep processes as analogs of rock salt creep processes: we used the microscropic description of grain rearrangement to model crack opening and closure, and grain cementation to model crack rebonding. We modeled microscopic cracks as oblate spheroids, oriented perpendicular to the loading axis, as shown in Figure 6. We established a closed formulation relating microstructure changes to phenomenological variables as follows:

- During elastic loading or unloading, only crack aperture varies
- When damage occurs, the crack length increases.
- Healing only occurs when the deformation in the loading direction is compressive. During healing, the crack length decreases whereas the aperture remains constant.

Table 2. Relations between microscopic and macroscopic variables.

Relation between fabric descriptor and phenomenological variables	
$\boldsymbol{R}$ and $\boldsymbol{A}$	$\boldsymbol{A} = \sum_{j=1}^{3} A_j e_j \otimes e_j,\ A_1 = N_v \frac{(\overline{R_2}\cdot\overline{R_3})^{3/2}}{V_{REV}},\ A_2 = N_v \frac{(\overline{R_1}\cdot\overline{R_3})^{3/2}}{V_{REV}},\ A_3 = N_v \frac{(\overline{R_1}\cdot\overline{R_2})^{3/2}}{V_{REV}}$ $\overline{R_j} = \int R_j p_j(R_j) dR_j$
n_{3D} and A_v	$\frac{n_{3D} - n_{3D,lower}}{n_{3D,upper} - n_{3D,lower}} = \frac{n_{2D} - n_{2D,lower}}{n_{2D,upper} - n_{2D,lower}}$ $n_{2D,lower} = \frac{A_{v,lower}}{A_{REV}} = \frac{\pi r^2}{l^2},\ n_{3D,lower} = \frac{V_{v,lower}}{V_{REV}} = \frac{\frac{4}{3}\pi r^3}{l^3}$ $n_{2D,upper} = \frac{A_{v,upper}}{A_T},\ n_{3D,upper} = \frac{V_{v,upper}}{V_T},\ V_{v,upper} = V_T - V_s = A_{tube} \cdot L_{upper} - \frac{m_s}{\rho_s}$ $\overline{n_{2D}} = \int \frac{A_v}{A_{REV}} p_A(A_v) dA$
Relation between fabric descriptor and residual stress	
σ_R and R, A_v	$\sigma_R = N_v \sigma_r = N_v \frac{2\sqrt{2}}{\pi} \frac{\mu}{\kappa + 1} \frac{A_v}{R^2}$

$\overline{R_j}$	=	Mean value of crack length	A_j	=	Net damage in principal direction j
$n_{2D,lower}$	=	Lower bound of 2D porosity	V_{REV}	=	Volume of REV
$n_{3D,lower}$	=	Lower bound of 3D porosity	σ_R	=	Macroscopic residual stress for N_v cracks
$n_{2D,upper}$	=	Upper bound of 2D porosity	σ_r	=	Macroscopic residual stress for single crack
$n_{3D,upper}$	=	Upper bound of 3D porosity	A_T	=	Longitudinal cross-sectional area of the cylinder
V_s	=	Volume of the salt solid	V_T	=	Total volume of the sample cylinder
ρ_s	=	Density of the salt solid	A_v	=	Void area
m_s	=	Mass of the salt solid	A_{tube}	=	Inner cross-sectional area of tube

The space average of the density of net damage ($\bar{u}(t)$) is given in Table 1. According to the work of Weertman (1955), the diffusion coefficient D_c depends on both pressure and temperature. More activation energy is required for a chloride ion to jump into a chloride vacancy than for a sodium ion to jump into a sodium ion vacancy (Mapother et al. 1950). Hence we assumed that the migration of sodium ions dominates the diffusion of chloride. According to Mapother's (1950) study (temperature

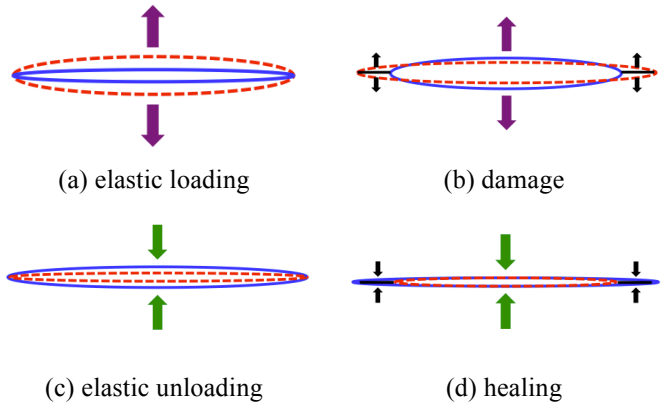

Figure 6. Evolution of microscopic crack geometry at different stages (model assumption).

We adopted the concept of crack density tensor (Kachanov 1992) to consider the difference of crack length in the three directions of space. Assuming that the principal directions of stress and net damage are parallel, net damage eigenvalues ($\boldsymbol{A}$) are related to the means of the crack length components (R_j) as presented in Table 2. Standard deviations did not vary significantly under the pressure and temperature conditions of the creep tests, hence we took constant standard deviations in the model. Only the means m_i were updated, following the same approach as Arson & Pereira (2013). The method to update the probability density function of R_j from the macroscopic strain is

$$\Delta\varepsilon \overset{Table\ 1}{\rightrightarrows} \Delta\boldsymbol{A} \overset{Table\ 2}{\rightrightarrows} \boldsymbol{R} \overset{Table\ 2}{\rightrightarrows} p_j(R_j). \tag{10}$$

Changes in three-dimensional void space could not be captured by our two-dimensional microscopic observations. We performed a linear interpolation to correlate 3D porosity with 2D porosity. Salt grains tend to rearrange and form an ordered pattern. However, voids exist even at maximum packing, because particles do not have a perfect cubic shape. We obtained the lower bound of porosities by assuming that inter-granular voids are spheres (details are available in (Zhu & Arson 2014b)). The upper bound of porosity is reached at the initial stage, when salt particles are assembled in loose packing before creep test starts. Given the lower and upper bounds of 2D and 3D porosities, the probability density function of void area was updated as

$$\Delta\varepsilon \rightarrow \Delta n_{3D} \overset{Table\ 2}{\rightrightarrows} \Delta n_{2D} \overset{Table\ 2}{\rightrightarrows} p_A(A_v). \tag{11}$$

2D porosities were calculated thanks to data provided by microscopic observations. 3D porosities were approximated from experimental measures of sample deformation (grains were considered incompressible, so that the volume change of the REV was taken equal to the porosity change).

Using the strain decomposition indicated in Figure 1, we expressed the stress tensor as

$$\boldsymbol{\sigma} = \boldsymbol{D}(\boldsymbol{\Omega}) : \boldsymbol{\varepsilon}^{\boldsymbol{E}} - \tau\boldsymbol{K}(\boldsymbol{\Omega}). \tag{12}$$

The stress rate under isothermal conditions is

$$\begin{aligned} d\boldsymbol{\sigma} &= \boldsymbol{D}(\boldsymbol{\Omega}) : d\boldsymbol{\varepsilon} + \frac{\partial \boldsymbol{D}(\boldsymbol{\Omega})}{\partial \boldsymbol{\Omega}} : \boldsymbol{\varepsilon} : d\boldsymbol{\Omega} \\ &\quad - d\left[\boldsymbol{D}(\boldsymbol{\Omega}) : \boldsymbol{\varepsilon}^{\boldsymbol{id}}\right] \\ &= \boldsymbol{D}(\boldsymbol{\Omega}) : d\boldsymbol{\varepsilon} + \frac{\partial \boldsymbol{D}(\boldsymbol{\Omega})}{\partial \boldsymbol{\Omega}} : \boldsymbol{\varepsilon} : d\boldsymbol{\Omega} + d\boldsymbol{\sigma}_{\boldsymbol{R}}. \end{aligned} \tag{13}$$

We considered that micro-cracks did not interact, so that the solid matrix surrounding each crack could be considered as an isotropic linear elastic material. We used the theory of fracture mechanics (Anderson 2005) to compute the micro-crack opening vector of an ellipsoidal micro-crack propagating in mode I. The micro-crack displacement in the direction perpendicular to the micro-crack axis is

$$u_y(r,\theta) = \frac{K_I}{2\mu}\sqrt{\frac{r}{2\pi}}\sin\left(\frac{\theta}{2}\right)\left[\kappa + 1 - 2\cos^2\left(\frac{\theta}{2}\right)\right], \tag{14}$$

in which u_y is half of the crack aperture at location (r,θ), K_I is the stress intensity factor in mode I at the crack tip ($r = 0$), and μ is the shear modulus of the linear elastic bulk material. κ depends on the bulk Poisson's ratio ν.

K_I is a function of the microscopic residual stress that applies to the micro-crack faces: $K_I = \sigma_r\sqrt{\pi R}$. The half aperture $0.5\lambda_a$ defined above is equal to the displacement u_y when $\theta = \pi$, and $r = R$, in which R is half of the crack length as

$$\frac{1}{2}\lambda_a = \frac{\kappa+1}{2\sqrt{2}\mu} R\sigma_r. \tag{15}$$

For ellipsoidal cracks, the void area can be calculated as $A_v = 0.5\pi\lambda_a R$. The combination of Equations 14 and 15 provided the macroscopic residual stress for N_v micro-cracks (Table 2).

The probability density functions of fabric descriptors were then updated with deformation and damage (Equations (10) and (11)), and the residual stress could be updated based on those descriptors (see (Zhu & Arson 2014b) for more details).

The relations between fabric descriptors and macroscopic variables are summarized in Table 2. Figure 7 describes the computational method used to update macroscopic variables from the knowledge of microscopic descriptors.

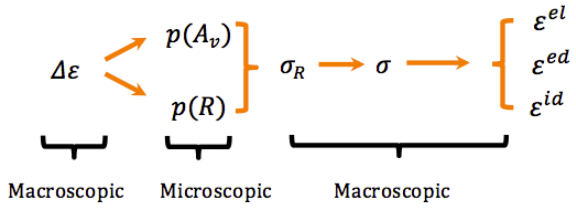

Figure 7. Computation method to correlate macroscopic variables with microscopic descriptors.

4 NUMERICAL SIMULATION

We carried out numerical simulations at one material point in MATLAB to assess the effect of healing on the performance of salt cavities used for CAES. The simulation comprises four phases, representing one typical CAES loading-unloading cycle (Fig. 8):
(1) Pressurization under injection pressure P_1. Tensile damage propagates in the radial direction at the wall of the cavity.
(2) De-pressurization under injection pressure P_2 (P_2<P_1). Cracks are under compression. We can assume that cracks close completely.
(3) Healing at high temperature. Under compression with elevated temperature, closed cracks rebond.
(4) Re-pressurization of the cavity under injection pressure P_3 (P_3>P_1). Re-pressurization at a lower pressure than in phase 1 does not reopen the rebonded cracks or generate new cracks.

The Kirsch (1898) equations are used to determine the hoop stress around the cavity. Taking compression as positive and assuming an isotropic far-field stress, the hoop stress $\sigma_{\theta\theta}$ is computed as

$$\sigma_{\theta\theta} = 2\sigma_f - P_i, \quad (16)$$

where P_i is the internal pressure, σ_f is the far-field stress.

Let us consider a typical geological storage site in salt rock located at a depth of 300 m, the hydrostatic stress can be approximated as

$$\sigma_f = \gamma z = 2.5\times\frac{10^3 kg}{m^3}\times\frac{10N}{kg}\times 300m = 7.5MPa. \quad (17)$$

The material element considered in the following is a stress element located at the cavity wall. The uniaxial stress imposed in the simulation at the material element level is taken equal to the deviatoric stress that develops at the cavity wall:

$$\sigma_n = \sigma_{\theta\theta} - \sigma_{rr} = 2\sigma_f - P_i - \sigma_{rr} = 2(\sigma_f - P_i). \quad (18)$$

The stress path simulated comprises loading, unloading, healing and reloading phases. We chose three injection pressures: P_1 = 20MPa, P_2 = 5MPa, P_3 = 25MPa. The resulting deviatoric stresses are σ_{n1}= -25MPa (tension), σ_{n2} = 5MPa (compression), σ_{n3}= -35MPa (tension).

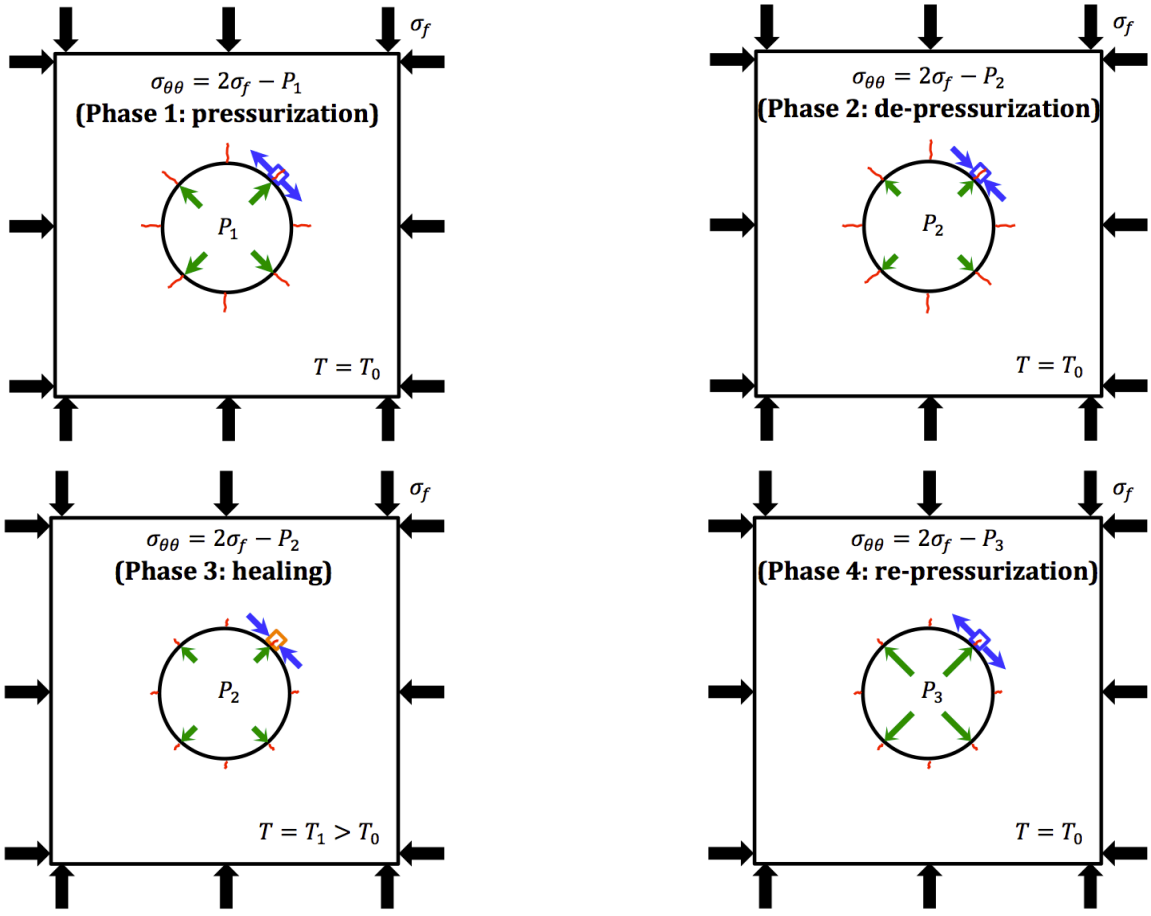

Figure 8. Simulation of damage and healing around a salt cavity.

The macroscopic damage and healing model depends on seven mechanical parameters and one thermal parameter. To the authors' best knowledge, experimental data is not available to calibrate the anisotropic damage parameter for salt rock. For illustrative purposes, a set of parameters fitted for sandstone was used. The microscopic parameters were chosen according to (Maleki 2004). Model parameters in the simulation are summarized in Table 3.

Table 3. Model parameters used for the strain-controlled uniaxial test with soil mechanics sign convention.

λ (Pa)	μ (Pa)	α (Pa)	β (Pa)
2.63e10	1.75e10	1.9e9	-2.04e10
g (Pa)	C_0 (Pa)	C_1 (Pa)	α_T (K^{-1})
1.1e8	200	1e5	-1e-5
U_0 (-)	l (m)	e_0 (-)	t (-)
1	1e-4	0.008	-1.2
$n_{2D,lower}$ (-)	$n_{2D,upper}$ (-)	$n_{3D,lower}$ (-)	$n_{3D,upper}$ (-)
0.03	0.165	0.004	0.321
R_{min} (m)	R_{max} (m)	A_{min} (m^2)	A_{max} (m^2)
1e-6	1e-5	1e-14	1e-12

Given the initial damage induced by pressurization P_1 and the pressure P_3 as the injection pressure used for geological storage, we can calculate the minimum value of the healing variable necessary to avoid crack propagation during phase 4 (injection for geological purposes). Towards this goal, we simulated two scenarios leading to crack rebonding during phase 3: long-term healing at low temperature, and short-term healing at high temperature. The simulation plan is summarized in Table 4. Scenario 1 is the reference case, without healing.

Table 4. Simulation plan for two healing scenarios

Scenario	T_1 (K)	t_{heal} (s)	D_C (m^2/s)
1	293	0	-
2	593	2×10^5	1.74×10^{-16}
3	633	1×10^5	3.52×10^{-16}

The stress-strain curve (Fig. 9a) follows the expected trends shown in Figure 1. In phase 1, the response is elastic (OA) before damage initiation (at point A). Cumulated damage degrades the stiffness until unloading starts (AB). All tensile stresses are released (BC) during phase 2. Additional compression closes all cracks (CD) and the unilateral effects result in stiffness recovery under compression (DE). Healing occurs in Phase 3 at an elevated temperature (EF). During Phase 4, tensile deformation starts after decreasing the temperature and reloading (FG). Additional damage is produced after recovery (GH) when the new damage threshold is reached.

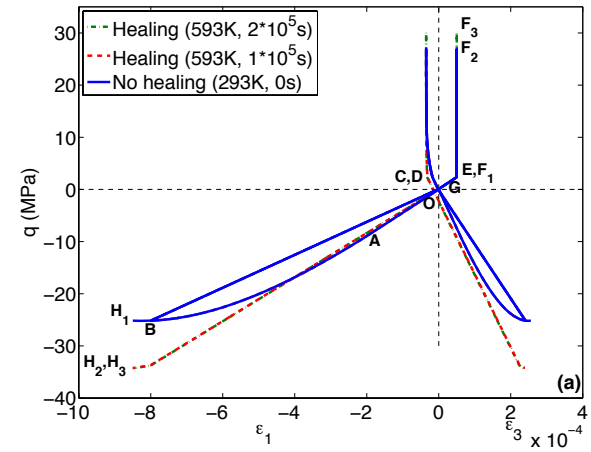

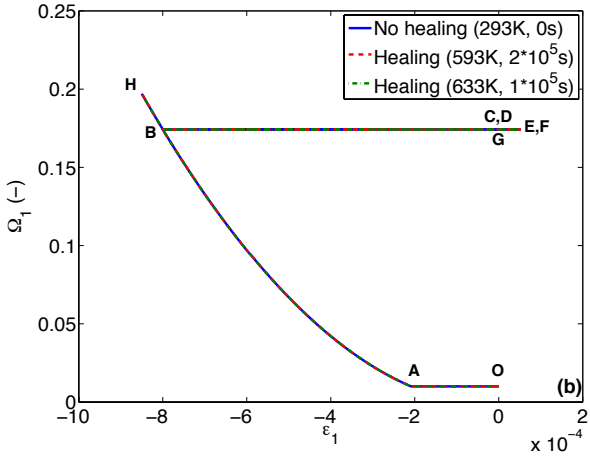

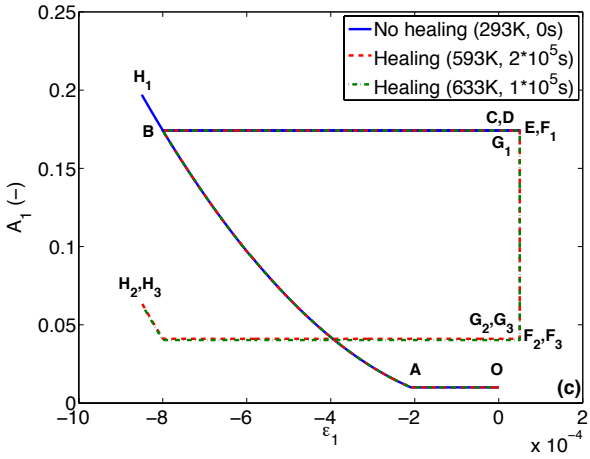

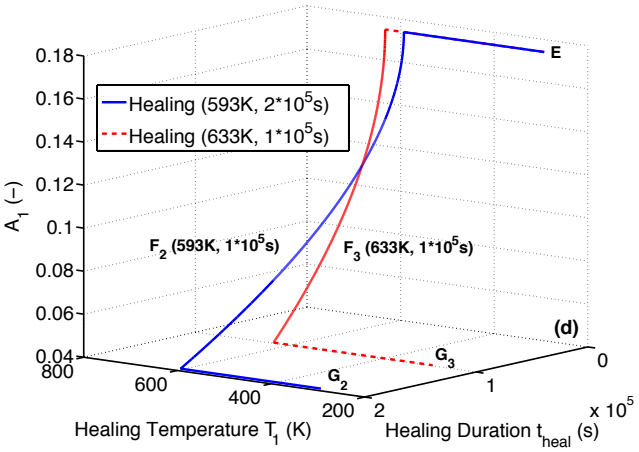

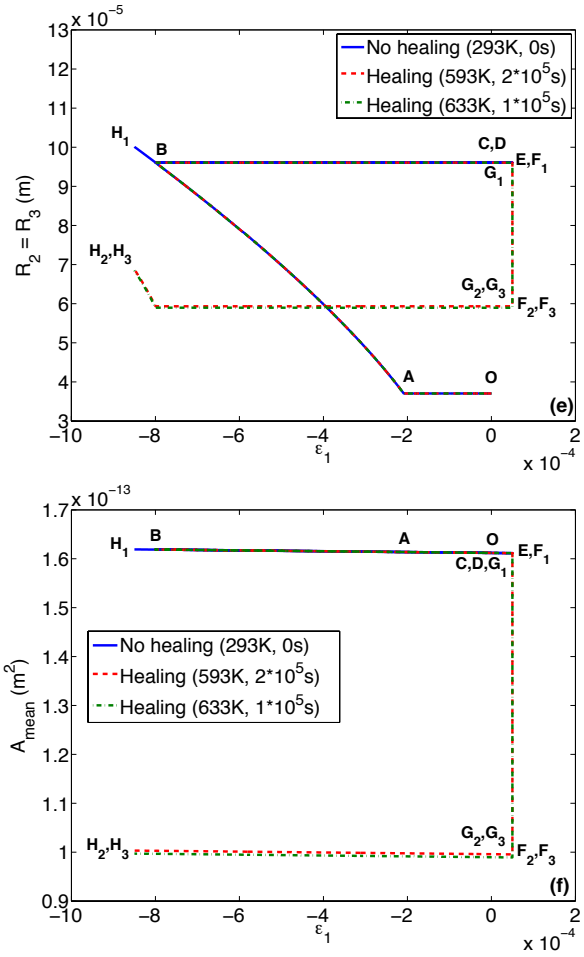

Figure 9. Influence of healing time/temperature on mechanical recovery: (a) stress-strain curve, (b) evolution of the damage variable, (c) evolution of net damage, (d) evolution of net damage during the healing phase, (e) evolution of crack lengths, (f) evolution of the mean void area. Stress paths for the 3 scenarios are as follows: no healing (O-A-B-C-D-E-F_1-G_1-H_1), healing at 593K (O-A-B-C-D-E-F_2-G_2-H_2), and healing at 633K (O-A-B-C-D-E-F_3-G_3-H_3).

Figure 9b illustrates the evolution of the damage variable. Micro-cracks do not propagate during the elastic phase (OA) and the unloading phase (BCDE). The damage variable is time-independent and does not decrease. Therefore, it increases during the non-elastic tension phase (AB), remains constant during the healing phase (EF), and increases again during reloading (GH). Net damage evolution in Figure 9c is similar to the damage variable evolution, except that it decreases when healing occurs (EF). This is a result of crack rebonding during the creep process at constant axial deformation. When healing temperature is higher (increase from 593K to 633K), less time (drop from 2×10^5s to 1×10^5s) is needed for equivalent recovery (Fig. 9d).

Evolutions of fabric descriptors are presented in Figures 9e and 9f. Due to the axis-symmetry of the problem and by construction of the model, micro-cracks only propagate in planes orthogonal to the loading direction ($R_2 = R_3 \neq 0$, $R_1 = 0$). Since crack length is updated with net damage, evolution of crack length is similar to that of net damage.

The mean of void areas is proportional to the porosity of the sample, which is assumed to vary like the volumetric deformation. In the simulations, volumetric deformation is controlled by axial deformation, which is about three times larger than lateral deformation. The mean void area decreases during the healing phase, as crack lengths shorten and crack apertures remain constant.

5 CONCLUSION

We proposed a CDM model of damage and healing, which captures anisotropy of stiffness and deformation induced by crack debonding, opening, closure, and rebonding in salt rock. We expressed the free energy as a polynomial comprising a thermo-elastic component and a purely damaged energy component. We accounted for crack closure by introducing unilateral effects in the stiffness model, and we considered that DMT was the dominating mechanism driving crack rebonding. Based on microscopic observations of creep tests performed on table salt under constant stress and humidity conditions, we chose to relate CDM variables to microscopic descriptors defined from the probability density functions of the void area and the crack length.

We programmed the constitutive model at the integration point in MATLAB. We simulated the stress path undergone by a material element at the wall of a CAES cavity during one loading-unloading cycle. The loading phases included pressurization, de-pressurization, healing, and re-pressurization. Two scenarios leading to the same healing intensity were simulated: long-term healing at low temperature, and short-term healing at high temperature.

The model highlights the impact of time and temperature on stiffness recovery and healing efficiency. More experimental data is needed for proper model calibration in salt rock. Theoretical developments to account for diffusion at grain boundaries (and subsequent anisotropic healing) are underway. We expect this model to improve the fundamental understanding of damage and healing in salt rock at both macroscopic and microscopic levels, and to allow long-term assessment of geological storage facilities.

ACKNOWLEDGEMENT

The authors are grateful to Professor Santamarina at the Georgia Institute of Technology, who kindly gave access to his laboratory for microscope imaging, and made suggestions to improve the experimental set up. Financial support for this research was provided by the School of Civil and Environmental Engineering at the Georgia Institute of Technology, and by the National Science Foundation

(Grant No. CMMI-1362004/1361996).

REFERENCES

Abramoff, M.D., Magalhaes, P.J. & Ram, S.J. 2004. Image processing with ImageJ. *Biophotonics international.* 11(7): 36–42.

Anderson, T. 2005. Fracture Mechanics: Fundamentals *and Applications.* 3rd Edition. Taylor & Francis.

Arson, C. & Pereira, J.M. 2013. Influence of damage on pore size distribution and permeability of rocks. *International Journal for Numerical and Analytical Methods in Geomechanics.* 37: 810–831.

Arson, C., Xu, H. & Chester, F. 2012. On the definition of damage in time-dependent healing models for salt rock. Geotechnique Lett. 2(April-June): 67–71.

Chaboche, J.L. 1992. Damage induced anisotropy: on the difficulties associated with the active/passive unilateral condition. *Int. J. Damage. Mech*. 1(2): 148–171.

Collins, I. & Houlsby, G. 1997. Application of thermomechanical principles to the modelling of geotechnical materials. *Proceedings of the Royal Society of London Series A: Mathematical, Physical and Engineering Sciences*. 453(1964): 1975–2001.

Dragon, A., Halm, D. & D´esoyer, T. 2000. Anisotropic damage in quasi-brittle solids: modelling, computational issues and applications. *Comput Methods Appl Mech Eng* 183(3): 331–352.

Fam, M., Santamarina, J., & Dusseault, M. 1998. Wave-based monitoring processes in granular salt. *Journal of Environmental & Engineering Geophysics*. 3(1): 41-47.

Fuenkajorn, K. & Phueakphum, D. 2011. Laboratory assessment of healing of fractures in rock salt. *Bulletin of Engineering Geology and the Environment.* 70(4): 665-672.

Hou, Z.M. 2003. Mechanical and hydraulic behavior of rock slat in the excavation disturbed zone around underground facilities. *International Journal of Rock Mechanics and Mining Sciences*. 40(5): 725-738.

Houben, M.E., Hove, A.T., Peach, C.J., & Spiers, C.J. 2013. Crack healing in rocksalt via diffusion in adsorbed aqueous films: Microphysical modeling versus experiments. *Physics and Chemistry of the Earth, Parts A/B/C*. 64: 95-104.

Kachanov, M. 1992. Effective elastic properties of cracked solids: critical review of some basic concepts. *Appl. Mech. Rev*. 45(8): 304–335.

Kirsch, E.G. 1898. Die Theorie der Elastizität und die Bedürfnisse der Festigkeitslehre. *Zeitschrift des Vereines deutscher Ingenieure*. 42: 797-807.

Li, G. & Uppu, N. 2010. Shape memory polymer based self-healing syntactic foam: 3-D confined thermo-mechanical characterization. *Composites Science and Technology*. 70(9): 1419–1427.

Mapother, D., Crooks, H.N. & Maurer, R. 1950. Self-diffusion of sodium in sodium chloride and sodium bromide. *The Journal of Chemical Physics.* 18:1231.

Maleki, K. 2004. *Modélisation numérique du couplage entre l'endommagement et la perméabilité des roches – Application a l'étude des ouvrages de stockage souterrain.* PhD Thesis, Ecole Nationale des Ponts et Chaussées.

Senseny, P., Hansen, F., Russell, J., Carter, N., & Handin, J. 1992. Mechanical Behavior of rock salt: phenomenology and micromechanisms. *International Journal of Rock Mechanics and Mining Sciences & Geomechanics Abstracts*. 29(4): 607-619.

Weertman, J. 1955. Theory of steady-state creep based on dislocation climb. *Journal of Applied Physics*. 26(10): 1213–1217.

Wexler, A. & Hasegawa, S. 1954. Relative humidity temperature relationships of some saturated salt solutions in the temperature range 0^0C to 50^0C. *Journal of Research of the National Bureau of Standards*. 53(1): 19-26.

Zhu, C. & Arson, C. 2014a. A thermo-mechanical damage model for rock stiffness during anisotropic crack opening and closure. *Acta Geotechnica*. DOI: 10.1007/s11440-013-0281-0.

Zhu, C. & Arson, C. 2014b. A model of damage and healing coupling halite thermo-mechanical behavior to microstructure evolution. *Geotechnical and Geological Engineering, Special Issue: Thermo-hydro-mechanical behavior of soils and energy geostructures*. DOI: 10.1007/s10706-014-9797-9.